Ablation of PM20D1 reveals *N*-acyl amino acid control of metabolism and nociception

Jonathan Z. Long[a,b,1], Alexander M. Roche[a,b], Charles A. Berdan[c,d,e], Sharon M. Louie[c,d,e], Amanda J. Roberts[f], Katrin J. Svensson[a,b,1], Florence Y. Dou[a,b], Leslie A. Bateman[c,d,e], Amir I. Mina[g], Zhaoming Deng[g], Mark P. Jedrychowski[a,b], Hua Lin[h], Theodore M. Kamenecka[h], John M. Asara[i], Patrick R. Griffin[h], Alexander S. Banks[g], Daniel K. Nomura[c,d,e], and Bruce M. Spiegelman[a,b,2]

[a]Department of Cancer Biology, Dana–Farber Cancer Institute, Harvard Medical School, Boston, MA 02115; [b]Department of Cell Biology, Harvard Medical School, Boston, MA 02115; [c]Department of Chemistry, University of California, Berkeley, CA 94720; [d]Department of Molecular and Cell Biology, University of California, Berkeley, CA 94720; [e]Department of Nutritional Sciences and Toxicology, University of California, Berkeley, CA 94720; [f]Department of Neuroscience, The Scripps Research Institute, La Jolla, CA 92037; [g]Division of Endocrinology, Diabetes and Hypertension, Brigham and Women's Hospital, Boston, MA 02115; [h]Department of Molecular Therapeutics, The Scripps Research Institute, Jupiter, FL 33458; and [i]Department of Medicine, Beth Israel Deaconness Medical Center, Boston, MA 02115

Contributed by Bruce M. Spiegelman, June 11, 2018 (sent for review February 27, 2018; reviewed by David Julius and Alan R. Saltiel)

***N*-acyl amino acids (NAAs) are a structurally diverse class of bioactive signaling lipids whose endogenous functions have largely remained uncharacterized. To clarify the physiologic roles of NAAs, we generated mice deficient in the circulating enzyme peptidase M20 domain-containing 1 (PM20D1). Global PM20D1-KO mice have dramatically reduced NAA hydrolase/synthase activities in tissues and blood with concomitant bidirectional dysregulation of endogenous NAAs. Compared with control animals, PM20D1-KO mice exhibit a variety of metabolic and pain phenotypes, including insulin resistance, altered body temperature in cold, and antinociceptive behaviors. Guided by these phenotypes, we identify *N*-oleoyl-glutamine (C18:1-Gln) as a key PM20D1-regulated NAA. In addition to its mitochondrial uncoupling bioactivity, C18:1-Gln also antagonizes certain members of the transient receptor potential (TRP) calcium channels including TRPV1. Direct administration of C18:1-Gln to mice is sufficient to recapitulate a subset of phenotypes observed in PM20D1-KO animals. These data demonstrate that PM20D1 is a dominant enzymatic regulator of NAA levels in vivo and elucidate physiologic functions for NAA signaling in metabolism and nociception.**

PM20D1 | *N*-acyl amino acid | knockout | pain | metabolism

Bioactive lipids regulate diverse aspects of mammalian physiology. The magnitude and duration of their actions are controlled by both metabolic enzymes and receptor signaling. In addition to their homeostatic functions, bioactive lipid-signaling pathways have attracted considerable pharmaceutical interest for the treatment of a broad range of disorders. For instance, modulators of the sphingosine-1-phosphate receptor are used for the treatment of multiple sclerosis (1), cyclooxygenase inhibitors that block prostaglandin production are used for the treatment of pain (2), and endocannabinoid hydrolase inhibitors are in clinical development for neurological disorders (3). Other, less characterized families of bioactive lipids have also been detected in mammalian tissues. One such family is the *N*-acyl amino acids (NAAs). NAAs are a composed of a fatty acyl chain linked to an amino acid by an amide bond (4). Structurally, the NAAs are closely related to other fatty acid amides including anandamide (5), an endogenous ligand of the cannabinoid receptors, and the sleep-inducing lipid oleamide (6). More than 50 distinct species of NAAs have been found (7), underscoring the structural and functional diversity of this family of lipids.

To date, much of our knowledge regarding the function of NAAs is derived from pharmacologic studies of the lipids themselves in cells or animals. Individual members of this lipid family have putative roles in metabolism (8–10), pain sensation (11, 12), bone function (13), and vascular homeostasis (14, 15). However, the direct contribution of specific endogenous NAAs to these diverse physiologic processes remains unknown. This has largely been due to a lack of knowledge about the precise metabolic enzymes or receptors that modulate NAA signaling in vivo. For example, biosynthetic or degradative pathways for NAAs have been previously proposed (11), but direct genetic evidence (e.g., enzyme knockout) linking those biochemical pathways in the regulation of NAA levels in vivo has been lacking. Similarly, specific NAAs putatively interact with candidate receptors, including ion channels (16) and G protein-coupled receptors (17). However, to date, little functional evidence has been provided for the physiological relevance of those NAA–receptor interactions.

We recently discovered a previously unknown biochemical route to and from NAAs mediated by a poorly characterized enzyme called "peptidase M20 domain-containing 1" (PM20D1). PM20D1 was identified as a factor secreted by thermogenic adipose cells that catalyzes both the hydrolysis and condensation of NAAs to and from free fatty acids and free amino acids (8). Increased circulating PM20D1 in mice, accomplished by adeno-associated virus (AAV)-mediated transduction, dramatically elevates multiple circulating NAAs including *N*-oleoyl phenylalanine and *N*-oleoyl leucine, leading to augmented energy expenditure, reduced adiposity, and

Significance

Bioactive lipids control a wide variety of physiologic processes. We have recently identified a branch of bioactive lipid signaling mediated by *N*-acyl amino acids (NAAs) and the circulating enzyme peptidase M20 domain-containing 1 (PM20D1). Here we generate and characterize mice globally deficient in PM20D1. These PM20D1-KO mice have bidirectional changes in NAA levels in blood and tissues and exhibit a variety of metabolic and nociceptive phenotypes. Our findings elucidate the endogenous physiologic functions for NAA signaling in vivo and suggest PM20D1 inhibitors might be useful for the treatment of pain.

Author contributions: J.Z.L., P.R.G., A.S.B., D.K.N., and B.M.S. designed research; P.R.G., A.S.B., D.K.N., and B.M.S. supervised research; J.Z.L., A.M.R., C.A.B., S.M.L., A.J.R., K.J.S., F.Y.D., L.A.B., A.I.M., Z.D., M.P.J., and J.M.A. performed research; J.Z.L., A.M.R., H.L., and T.M.K. contributed new reagents/analytic tools; J.Z.L., A.M.R., C.A.B., S.M.L., A.J.R., A.I.M., and B.M.S. analyzed data; and J.Z.L., K.J.S., and B.M.S. wrote the paper.

Reviewers: D.J., University of California, San Francisco; and A.R.S., University of California, San Diego.

Conflict of interest statement: B.M.S. is a consultant for Calico Life Sciences, LLC.

[1]Present addresses: Department of Pathology, Stanford University School of Medicine, Stanford, CA 94305; and Stanford Chemistry, Engineering & Medicine for Human Health, Stanford University, Stanford, CA 94305.

[2]To whom correspondence should be addressed. Email: Bruce_Spiegelman@dfci.harvard.edu.

This article contains supporting information online at www.pnas.org/lookup/suppl/doi:10.1073/pnas.1803389115/-/DCSupplemental.

Published online July 2, 2018.

improved glucose homeostasis. Mechanistically, NAAs stimulate uncoupled mitochondrial respiration across multiple cell types independent of the presence of uncoupling protein 1 (UCP1). These gain-of-function viral experiments provide strong evidence that PM20D1 can regulate NAAs levels in vivo and further support a role for NAAs in metabolic homeostasis. However, these studies did not precisely define the endogenous functions of these lipids or of PM20D1 itself.

To clarify the physiologic roles of NAAs and of PM20D1, we have now generated whole-body PM20D1-KO mice. These studies establish a dominant role for PM20D1 in the bidirectional regulation of tissue and circulating NAAs. PM20D1-KO mice also illustrate the endogenous physiologic functions of NAAs in glucose homeostasis, energy metabolism, and pain sensation in vivo.

Results

Generation of Whole-Body PM20D1-KO Mice. In addition to its expression in thermogenic adipocytes, PM20D1 is also highly expressed in other tissues including liver, pancreas, and kidney (Dataset S1). Because individual tissue-specific knockouts might not reduce the bulk circulating pool of PM20D1, we generated mice lacking PM20D1 in all tissues (global PM20D1-KO mice). A CRISPR-Cas9 approach was used to target the first exon of the *Pm20d1* gene (*Methods*). Of the 42 injected embryos, two pups were recovered with genome modifications. One pup harbored a 6-bp out-of-frame deletion (Δ6-bp) in exon 1 which fortuitously resulted in the conversion of a phenylalanine codon (TTC) into a premature stop codon (TAG) (Fig. 1*A*). Sanger sequencing confirmed the presence of a new T–A junction and a new stop codon (Fig. 1*B*). qPCR primers that specifically anneal WT *Pm20d1* but not the Δ6-bp allele failed to amplified a signal from PM20D1-KO mice (Fig. 1*C*), demonstrating that the Δ6-bp modification was also present in *Pm20d1* mRNA from PM20D1-KO mice. To evaluate the effect of the predicted early stop codon on PM20D1 protein levels, we performed quantitative shotgun proteomics analysis of whole livers from PM20D1-KO and WT littermates using tandem mass tag (TMT) labeling (*Methods*). In total, 216 proteins with at least two independent peptides per protein were detected (Dataset S2). PM20D1 protein levels were completely abolished in PM20D1-KO mice (>99.99% reduced versus WT mice) (Fig. 1*E*). In contrast, all remaining 215 proteins in PM20D1-KO mice were found to be within approximately twofold of WT levels (Fig. 1*E* and Dataset S1). Taken together, these data validate the specific loss of PM20D1 protein in the PM20D1-KO mouse model generated here.

Dramatically Reduced NAA Synthase/Hydrolase Activity in PM20D1-KO Tissues. PM20D1-KO mice were viable, fertile, and born in the expected Mendelian ratios from heterozygous breeding crosses. They were also normal in their home cage behavior and overtly indistinguishable from WT littermates. We assessed NAA hydrolysis activity in plasma from WT and PM20D1-KO mice using a prototypical NAA substrate, *N*-arachidonoyl glycine (C20:4-Gly). Under our reaction conditions, WT plasma showed 44 ± 4% conversion of the starting material into the arachidonic acid product. Remarkably, this activity was completely abolished in PM20D1-KO plasma (>99% reduction versus WT plasma; $P < 0.001$) (Fig. 1*F*). Dramatic reductions in NAA hydrolysis activity were observed in other tissues from PM20D1-KO versus WT mice (Fig. 1*F*). On average across all tissues, PM20D1-KO mice possessed only 16 ± 4% of the WT C20:4-Gly hydrolysis activity. Moreover, the hydrolysis activity attributable to PM20D1 in terms of percent conversion was remarkably consistent with the known expression of PM20D1. For instance, no NAA hydrolysis activity was detected in quadriceps, consistent with the lack of PM20D1 expression in this tissue (Dataset S1). Conversely, significantly higher NAA hydrolysis rates were observed in brown adipose tissue (BAT) versus the inguinal white

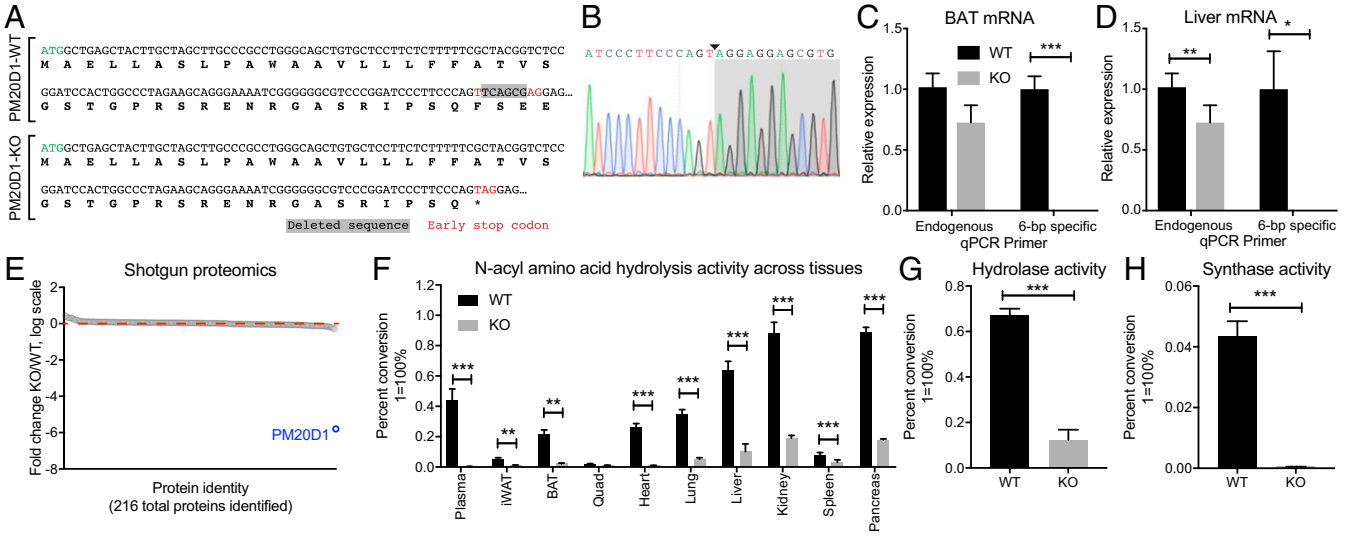

Fig. 1. Generation of the PM20D1-KO mouse and loss of NAA hydrolase/synthase activity in PM20D1-KO tissues. (*A*) Nucleotide and predicted protein sequence for the *Pm20d1* gene from WT or PM20D1-KO animals. The Δ6-bp out-of-frame deletion is highlighted in gray, and the newly generated early stop codon is identified by red text. (*B*) Sanger sequencing chromatograms of a PCR product amplified from the *Pm20d1* gene in PM20D1-KO mice. The new A–T junction is identified by the arrowhead, and the 25-bp region flanking this junction is shown. (*C* and *D*) Relative levels of *Pm20d1* mRNA from BAT (*C*) and livers (*D*) of WT and PM20D1-KO mice using qPCR primers that anneal either downstream of the Δ6-bp deletion ("endogenous") or directly on the deleted wild-type sequence ("6-bp specific"). (*E*) Fold change in protein abundance of 216 proteins detected by quantitative shotgun proteomics from livers of WT and PM20D1-KO mice. The red dashed line indicates a fold change = 1 in KO versus WT mice. (*F*) Percent conversion of the starting material C20:4-Gly into an arachidonic acid product in the indicated tissues from WT or PM20D1-KO mice. (*G*) Percent conversion of the C18:1-Phe starting material into an oleate product in livers from WT and PM20D1-KO mice. Hydrolase reactions in *F* and *G* were performed by incubating 100 μg of whole-tissue lysate in 100 μL PBS with 100 μM of the indicated NAA for 1 h at 37 °C. (*H*) Percent conversion of the Phe starting materials into a C18:1-Phe product in livers from WT and PM20D1-KO mice. Synthase reactions were performed by incubating 100 μg of whole-liver lysate in 100 μL PBS with 100 μM Phe and 2 mM oleic acid for 1 h at 37 °C. Data are shown as means ± SEM; *$P < 0.05$, **$P < 0.01$, ***$P < 0.001$ for the indicated comparisons. For *C*, *D*, and *F*–*H*, $n = 4$ per group. For *E*, $n = 2$ per group.

adipose tissue (iWAT), consistent with the known enrichment of PM20D1 in thermogenic versus nonthermogenic adipocytes. Together, these data demonstrate that PM20D1 is the sole NAA hydrolase in plasma and is a dominant NAA hydrolase in other mouse tissues. Other unknown lipid amidases might contribute to the small residual hydrolysis activity observed in some PM20D1-KO tissues.

PM20D1 can also catalyze an NAA synthase reaction in vitro, condensing free amino acids and free fatty acids to generate NAAs. We therefore specifically examined both hydrolysis and synthesis directions in liver tissue using *N*-oleoyl phenylalanine (C18:1-Phe), oleate, and phenylalanine. In the hydrolysis direction, using C18:1-Phe as a starting material, WT livers showed a robust hydrolase activity that was strongly reduced in livers from PM20D1-KO mice (67 ± 3% conversion in WT versus 14 ± 4% in KO; $P < 0.001$) (Fig. 1*G*). In the synthase direction, using oleate and phenylalanine, WT livers exhibited robust condensation activity to generate C18:1-Phe (4.4 ± 0.5% conversion) which was completely abolished in PM20D1-KO livers (<0.1% conversion; $P < 0.01$) (Fig. 1*H*). These data establish PM20D1 as the dominant enzyme responsible for liver NAA synthase activity.

Bidirectional Dysregulation of Endogenous NAAs in PM20D1-KO Mice. We developed a targeted multiple reaction monitoring (MRM) mass spectrometry method to measure endogenous NAAs in blood and tissues from WT and PM20D1-KO mice. From the >200 distinct NAA species that could, in principle, be formed, we focused our initial analysis on the C18:1- and C20:4-containing NAAs because this subset captured both highly abundant (oleoyl) and structurally unusual (arachidonoyl) lipids. Targeted MRM measurements of blood revealed a remarkable tissue- and species-specific bidirectional dysregulation of NAAs in PM20D1-KO mice. For instance, C18:1-Gln/Lys, C18:1-Leu/Ile, and C20:4-Leu/Ile were all significantly elevated two- to fivefold in PM20D1-KO blood versus WT blood (Fig. 2*A*), while C20:4-Gly was simultaneously reduced by 65 ± 8% ($P < 0.05$) (Fig. 2*A*). In BAT, a different subset of NAAs was detected with distinct regulation compared with the circulating pools. C18:1-Gln/Lys was again significantly elevated ($P < 0.05$), while C20:4-Phe was 79 ± 8% reduced ($P < 0.01$) in PM20D1-KO versus WT mice (Fig. 2*B*). Last, in liver, multiple NAAs were dramatically elevated in KO animals (average fold change across all NAAs, 16 ± fivefold elevated in KO versus WT) (Fig. 2*C*). Absolute quantitation of metabolite levels in the PM20D1-KO mice revealed NAA levels of ∼10–500 pmol/g in various tissues and blood (Dataset S3).

The only consistent metabolite change observed across tissues was an increase in C18:1-Gln/Lys in PM20D1-KO mice versus WT mice (four ± onefold, three ± onefold, and nine ± twofold elevated in blood, BAT, and liver, respectively). Initially, it was difficult to determine whether one or both of these species (C18:1-Gly or C18:1-Lys) was elevated because they were isobaric at unit mass resolution (m/z = 409.31 and 409.34 for C18:1-Gln and C18:1-Lys, respectively), fragmented by the loss of the amino acid head group (m/z = 145.1 for both Lys and Gln), and coeluted under our chromatography conditions. However, a modified chromatographic protocol on a high-resolution mass spectrometry instrument could readily distinguish C18:1-Gln from C18:1-Lys by both retention times and masses (*Methods* and Fig. 2*D*). In both liver and BAT, endogenous C18:1-Gln was readily detected and dramatically elevated in PM20D1-KO versus WT mice. In contrast, no C18:1-Lys peak was observed under these conditions (Fig. 2*D*). These data establish that C18:1-Gln is consistently elevated across multiple tissues in PM20D1-KO mice.

Impaired Glucose Homeostasis in PM20D1-KO Mice. We next sought to use this mouse model to critically interrogate the endogenous function of the PM20D1-regulated NAAs. Because a considerable body of pharmacologic studies suggested putative NAA functions in metabolism (8–10, 18) and pain sensation (11, 12, 19), we focused our phenotypic characterization on these two physiological processes. We began by assessing whole-body metabolic parameters in PM20D1-KO and WT mice at room temperature using indirect calorimetry. On chow diet, body weights were not different between genotypes (23.5 ± 0.5 g in WT mice versus 24.1 ± 0.6 g in KO mice; $P > 0.05$). Energy expenditure, oxygen consumption (VO_2), carbon dioxide production (VCO_2), and food intake were also indistinguishable between genotypes, while

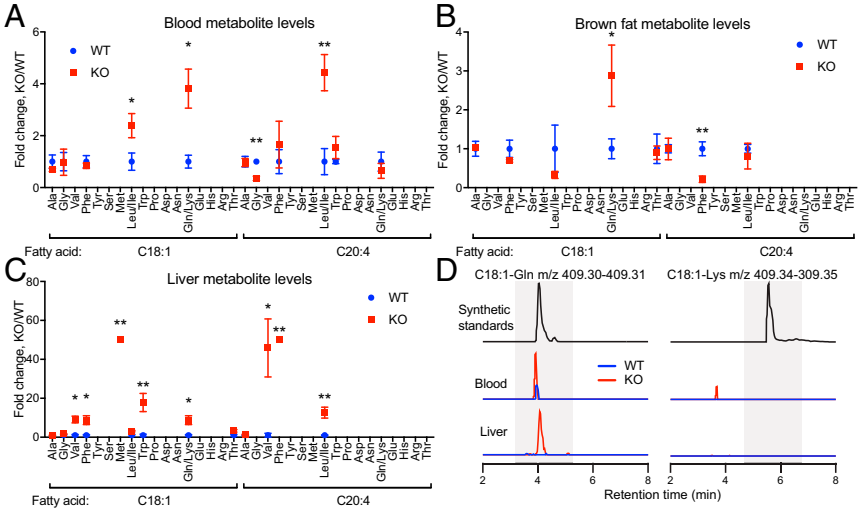

Fig. 2. Bidirectional dysregulation of endogenous NAAs in tissues from PM20D1-KO mice. (*A*–*C*) Relative levels of the indicated NAA metabolites in blood (*A*), BAT (*B*), or liver (*C*) of WT or PM20D1-KO mice. Metabolites were extracted in using acetonitrile/methanol/water and were analyzed in targeted mode by MRM in unit mass mode. NAAs that were not detected are not shown. For NAAs detected in PM20D1-KO mice for which no corresponding peak was detected in WT mice, the fold change was set to 50. Data are shown as means ± SEM; *$P < 0.05$, **$P < 0.01$ for the indicated metabolite in WT versus PM20D1-KO mice; $n = 4$ per group. (*D*) Representative extracted ion chromatograms (EICs) of the peaks corresponding to C18:1-Gln and C18:1-Lys in blood and liver from WT and PM20D1-KO mice using alternative chromatographic conditions on a high-resolution mass spectrometer (*Methods*). EICs for the $[M-H]^-$ ion were extracted with the indicated mass window, and standards were chemically synthesized as described in *Methods*. The background in gray indicates the elution time of the C18:1-Gln or C18:1-Lys standard ±1 min.

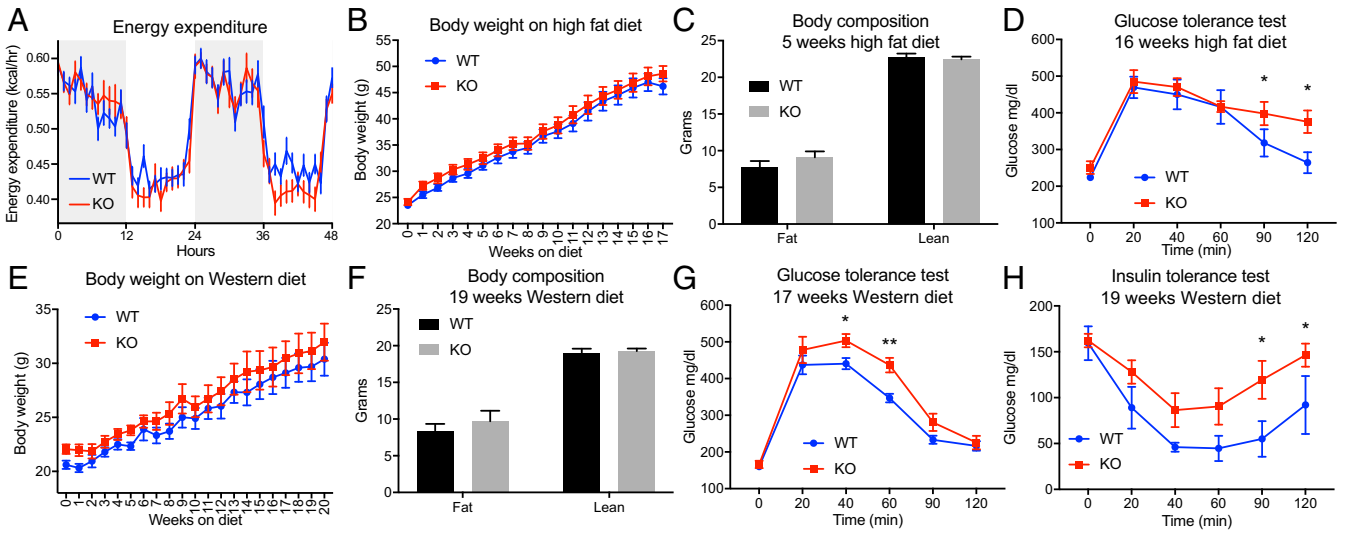

Fig. 3. Glucose intolerance and reduced insulin sensitivity in PM20D1-KO mice. (*A*) Whole-body energy expenditure of 8- to 10-wk-old male WT and PM20D1-KO mice over 2 d on a chow diet. Gray background indicates nighttime and white background indicates daytime. (*B–D*) Total body weights (*B*), lean and fat mass (*C*), and glucose tolerance test (*D*) of male WT and PM20D1-KO mice on an HFD (60% kcal from fat) starting at 6–10 wk of age. In *C* and *D*, body composition (*C*) was measured at 5 wk on the HFD, and the glucose tolerance test (*D*) was administered at 17 wk on the HFD. (*E–H*) Total body weights (*E*), lean and fat mass (*F*), glucose tolerance (*G*), and insulin tolerance (*H*) of female WT and PM20D1-KO mice on a Western diet (40% kcal from fat, 0.2% cholesterol) starting at 12–16 wk of age. For *F–H*, body composition was measured (*F*) and the insulin tolerance test was administered (*H*) at 19 wk on the Western diet, and the glucose tolerance test (*G*) was administered at 17 wk on the Western diet. Data are shown as means ± SEM; $^*P < 0.05$, $^{**}P < 0.01$ for WT versus PM20D1-KO. $n = 8$–13 per group in *A–D*, and $n = 6$ per group in for *E–H*.

locomotor activity and resting energy requirements (RER) were slightly increased and decreased, respectively, in PM20D1-KO mice (Fig. 3*A* and *SI Appendix*, Fig. S1). Glucose and insulin tolerance tests demonstrated unaltered glucose homeostasis in genotypes under basal, chow-diet conditions (*SI Appendix*, Fig. S2). Next, a cohort of PM20D1-KO and littermate WT control mice were placed on a high-fat diet (HFD; 60% kcal from fat) to induce a metabolic stress that produces obesity and insulin resistance. Over 4 mo on HFD, body weights did not differ between genotypes although the PM20D1-KO mice consistently trended toward slightly heavier weights throughout the experiment (final weights: 46.2 ± 1.5 g in WT mice vs. 48.6 ± 1.5 g in KO mice; $P > 0.05$) (Fig. 3*B*). Fat and lean mass as assessed by MRI were indistinguishable between genotypes (Fig. 3*C*). After 16 wk of HFD feeding, PM20D1-KO mice exhibited worsened glucose tolerance than WT control mice (Fig. 3*D*). To provide a distinct metabolic dietary stressor, we challenged a new cohort of PM20D1 WT and -KO mice with Western diet (40% kcal from fat, 0.2% cholesterol). Body weight, while not statistically significant between genotypes (Fig. 3*E*), once again trended toward higher weights in the PM20D1-KO mice (final weights: 30.4 ± 1.5 g in WT mice vs. 32.0 ± 1.7 g in KO mice; $P > 0.05$). Adiposity also did not differ between genotypes at the end of the diet treatment (Fig. 3*F*). Nevertheless, after 17 wk of Western diet, PM20D1-KO mice exhibited a marked impairment in glucose homeostasis, similar to that previously observed following prolonged HFD (Fig. 3*G*). At 19 wk, an insulin tolerance test also revealed markedly reduced insulin sensitivity in PM20D1-KO mice compared with WT mice (Fig. 3*H*). Taken together, these results demonstrate that PM20D1-regulated NAAs play a significant role in glucose homeostasis and insulin sensitivity under diet-induced obesity conditions while having no major effects on body weight or adiposity.

Augmented Defense of Body Temperature in PM20D1-KO Mice. Because NAAs can function as endogenous mitochondrial uncouplers and increased in the circulation following cold exposure (8), we next evaluated the body temperature responses of PM20D1-KO mice to an environmental cold challenge. H&E staining revealed morphologically similar BAT between genotypes (Fig. 4*A*). Basal body temperature was indistinguishable between genotypes at room temperature as assessed by rectal thermometer (38.3 ± 0.1 °C in WT versus 38.5 ± 0.1 °C in KO mice; $P > 0.05$). When mice were transferred to 4 °C, the rectal temperatures of PM20D1-WT mice dropped to 34.3 ± 0.4 °C following cold exposure before stabilizing at 36.4 ± 0.3 °C by the end of the experiment (Fig. 4*B*). In contrast, PM20D1-KO mice maintained average rectal temperatures 0.7 ± 0.1 °C higher than WT mice throughout this time course ($P < 0.01$) (Fig. 4*B*). We measured body temperature following cold exposure in a separate cohort of mice with telemetry temperature sensors implanted in the intraperitoneal cavity. During the cold exposure, PM20D1-KO mice were once again 0.7 °C warmer than WT mice (averages: 35.3 ± 0.1 °C in KO mice and 34.6 ± 0.1 °C in WT mice; $P < 0.01$). These temperature differences occurred in the absence of any changes in a panel of mitochondrial proteins or UCP1 protein levels in the BAT or the iWAT (Fig. 4 *D* and *E*). Similarly, PM20D1-KO mice did not have any increases in genes corresponding to alternative adipose futile cycling pathways, including creatine cycling and sarco/endoplasmic reticulum Ca^{2+}-ATPase (SERCA) cycling (Fig. 4 *F* and *G*). Taken together, these data implicate PM20D1-regulated NAAs in the defense of body temperature independent of any changes in known thermogenic programs.

Antinociceptive Behaviors in PM20D1-KO Mice. Besides functions in metabolism, a subset of NAAs containing glycine head groups (e.g., C20:4-Gly and C16:0-Gly) also have putative antinociceptive functions in inflammatory (11), neuropathic (20), and thermal (12) pain models. However, whether non–Gly-containing NAAs, such as those dysregulated in PM20D1-KO mice, might also function in pain sensation remained unknown. We first assessed acute thermal pain sensation using the tail flick assay. In this assay, a light beam that acts as a radiant heat stimulus is applied to the tail, and the latency to flicking the tail is measured. Both genotypes exhibited similar latency responses (Fig. 5*A*). Similarly, in the hot plate assay for acute thermal pain, both genotypes exhibited similar latency to a nociceptive response (hind paw lick, flick, or jump) in response

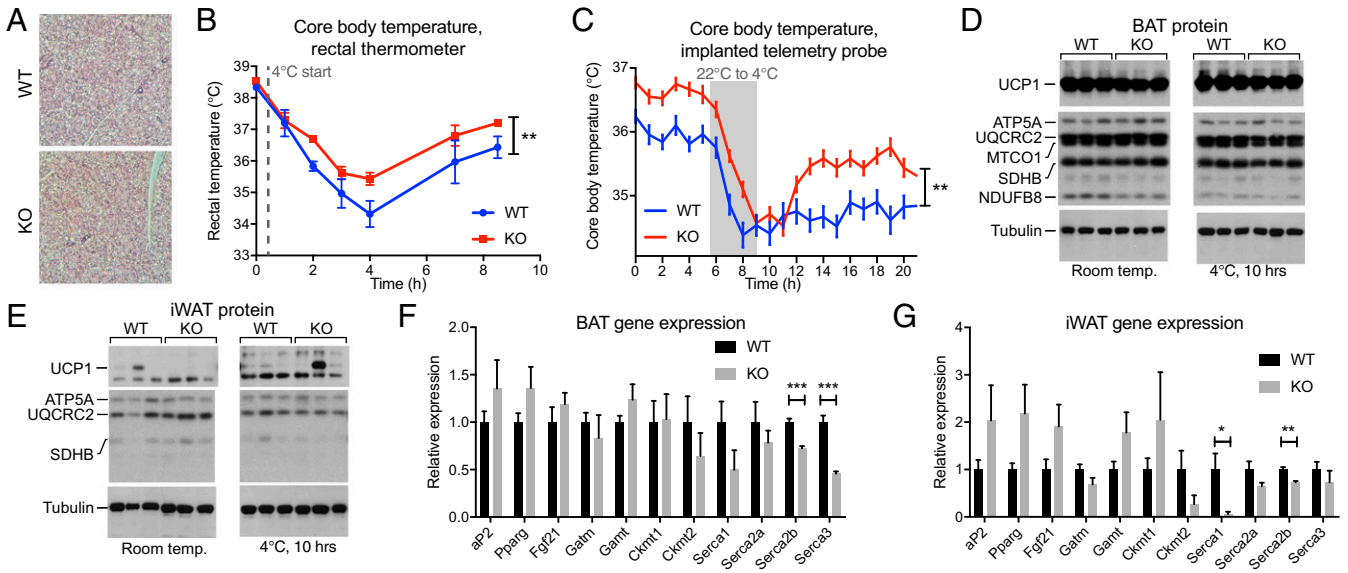

Fig. 4. PM20D1 mice maintain a higher body temperature following cold exposure. (*A*) Representative BAT sections stained with H&E from WT and PM20D1-KO mice. (Magnification: 10×.) (*B* and *C*) Core body temperatures at room temperature and after transfer to 4 °C as measured by rectal thermometer (*B*) or telemetry probe implanted into the i.p. cavity (*C*) in WT and PM20D1-KO mice. Immediate transition from room temperature to 4 °C is indicated by the dashed gray line (*B*), and a slow transition over 3 h from room temperature to 4 °C is indicated by the gray bar (*C*). (*D* and *E*) Protein levels of UCP1, mitochondrial proteins, and tubulin in BAT (*D*) or iWAT (*E*) of WT and PM20D1-KO mice at room temperature or after 10 h at 4 °C. (*F* and *G*) mRNA levels of the indicated genes in WT and PM20D1-KO mice from BAT (*F*) or iWAT (*G*) at room temperature. All mice were males, 8–12 wk of age. Data are shown as means ± SEM; $*P < 0.05$, $**P < 0.01$, $***P < 0.001$. For *B* and *C*, $n = 6$–12 per group; for *F* and *G*, $n = 5$–6 per group.

to a 52 °C hot plate surface (Fig. 5*B*). Because thermal pain responses were normal in PM20D1-KO mice, we next measured pain responses to inflammatory and chemical stimuli using two previously established assays, the formalin assay and the acetic acid constriction test. Intraplantar injection of dilute formalin into the mouse paw produces a stereotypical biphasic response consisting of an initial, rapid burst of paw licking and lifting (0–10 min after injection) followed later by a slowly rising and long-lasting second phase of pain behaviors (10–60 min after injection). PM20D1-KO mice showed significantly reduced paw-licking time in the late phase but not in the early phase of the formalin assay (late phase: 215 ± 16 s in PM20D1-KO mice versus 254 ± 17 s in WT mice; $P < 0.05$) (Fig. 5*C*). Second, dilute acetic acid was administered i.p., and the number of stereotyped constriction

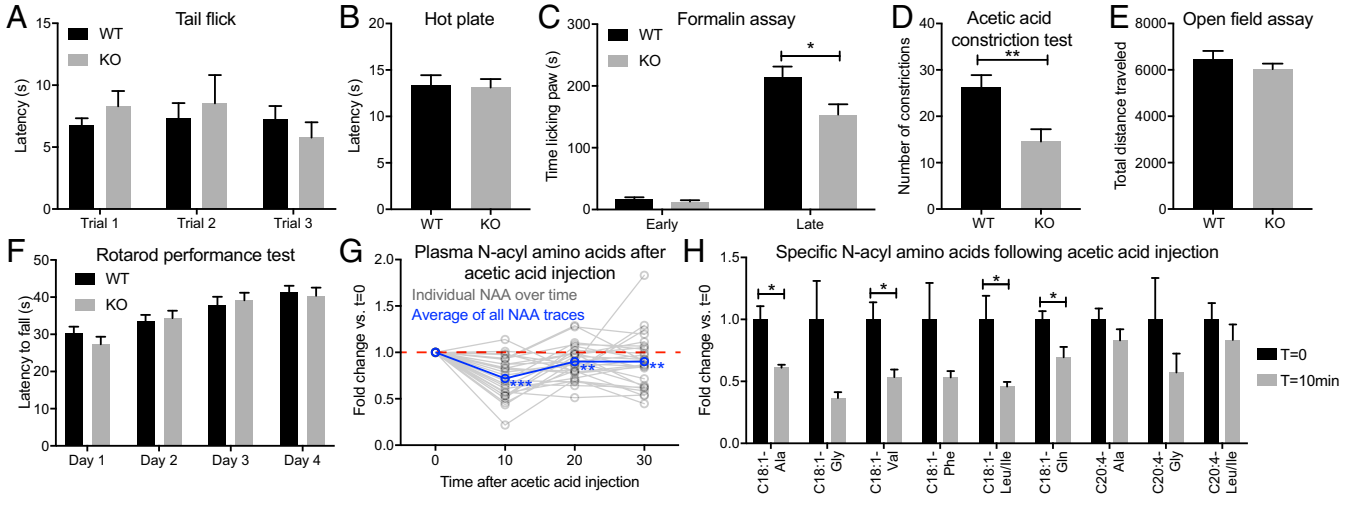

Fig. 5. Antinociceptive behaviors of PM20D1-KO mice in response to inflammatory and chemical pain. (*A* and *B*) Latency to a tail flick in response to a radiant heat stimulus (*A*) or latency to hind paw lick, flick, or jump in response to a 52 °C hot plate (*B*) in WT and PM20D1-KO mice. (*C*) Time spent licking the injected paw after intraplantar administration of 5% formalin (20 μL per paw) in WT and PM20D1-KO mice. The early and late phases were quantified during the 0- to 5-min and the 20- to 40-min periods, respectively, after formalin injection. (*D*) Number of abdominal constrictions over 30 min following i.p. injection of 0.6% acetic acid (0.3 mL per mouse) in WT and PM20D1-KO mice. (*E* and *F*) Total distance traveled during a 10-min open field assay (*E*) and latency to fall from a rotarod (*F*) in WT and PM20D1-KO mice. (*G* and *H*) Fold change of all plasma NAAs (*G*) or individual NAAs (*H*) following i.p. injection of 0.6% acetic acid (0.3 mL/mouse) in WT mice. For *G*, individual NAAs over time are shown in gray, and the average fold change across all measured NAAs is shown in blue ($***P < 0.001$ for the indicated time point versus $t = 0$). All mice were males between 10–15 wk of age. Data are shown as means ± SEM; $*P < 0.05$, $**P < 0.01$. For *A*–*D*, $n = 20$–26 per group; for *E* and *F*, $n = 11$–15 per group; for *G* and *H*, $n = 5$ per group.

behaviors was quantified. PM20D1-KO mice exhibited significantly reduced constriction behaviors compared with WT mice (15 ± 3 constrictions in PM20D1-KO mice versus 26 ± 3 in WT mice; $P < 0.01$) (Fig. 5*D*). PM20D1-KO and WT mice were indistinguishable in the open field and rotarod assays of movement and coordination, demonstrating that the differences in pain responses were not simply due to differences in motility (Fig. 5 *E* and *F*). Taken together, these data indicate that PM20D1-KO mice exhibit antinociceptive behaviors selectively in response to chemical and inflammatory pain stimuli while maintaining normal thermal pain sensation and normal movement.

The antinociceptive phenotypes of PM20D1-KO mice suggested that NAAs themselves might be physiologic regulators of pain sensation. To address this question, we measured NAAs in blood following i.p. administration of acetic acid to mice. The relative levels of circulating NAAs were reduced by an average of 27 ± 4%, 11 ± 3%, and 11 ± 5% at 10, 20, and 30 min post injection, respectively ($P < 0.001$ for each pairwise comparison versus $t = 0$), although there was a wide variation in the behavior of any specific NAAs over this time course (Fig. 5*G*). The relative changes in specific NAAs at $t = 0$ and $t = 10$ min are shown in Fig. 5*H*. Some NAAs, including C18:1-Gln, were significantly reduced at 10 min (31 ± 8% reduced versus $t = 0$; $P < 0.05$), whereas others (e.g., C20:4-Ala) remained unchanged. These data demonstrate that a subset of NAAs is decreased following acetic acid administration and may contribute to physiologic nociception.

Identification of PM20D1-Regulated C18:1-Gln as an Antagonist of TRPV1. We next focused on identifying the NAAs and mechanisms that could explain the antinociception phenotypes observed in the PM20D1-KO mice. We reasoned that such nociception mechanisms might be distinct from their chemical uncoupling bioactivity and could elucidate other polypharmacologic bioactivities of this lipid class. Three candidate pathways emerged based on their known functions in nociception and their potential to be regulated by bioactive lipids: cannabinoid receptors agonism, blockade of prostaglandin signaling, and antagonism of transient receptor potential (TRP) nociceptor channels. However, NAAs do not bind cannabinoid receptors (21), and administration of C18:1-Gln to mice did not produce catalepsy behavior classically associated with cannabinoid receptor agonism (*SI Appendix*, Fig. S3*A*). Furthermore, neither prostaglandin signaling by the major inflammatory prostanoid PGE_2 nor COX enzyme activity was inhibited by pretreatment with various NAAs (*SI Appendix*, Fig. S3 *B–E*).

A subset of TRP channels, including TRPV1, TRPV3, TRPV4, and TRPA1, regulates nociception. Pharmacological antagonism of this subset is being pursued for the treatment of pain (22–25). To explore whether NAAs elevated in PM20D1-KO mice might antagonize TRP ion channel function, a fluorescence-based calcium imaging assay for quantifying TRPV1-mediated calcium flux was established (26). HEK293A cells were cotransfected with plasmids for TRPV1 and red fluorescent protein (RFP). After 2 d, cells were loaded with the calcium indicator Fluo-4 AM and were imaged following treatment with various compounds. As expected, capsaicin treatment induced a robust increase in the intracellular calcium concentration in the TRPV1-transfected, RFP^+ cells but not in untransfected, RFP^- cells (Fig. 6*A*). None of the NAAs tested produced robust calcium transients in TRPV1-transfected cells, demonstrating that they do not act as direct TRPV1 agonists (Fig. 6*B*). In contrast, upon preincubation with C18:1-Gln (50 μM, 2 min), the capsaicin-induced TRPV1 calcium response was nearly completely abolished (91 ± 3% reduction in C18:1-Gln pretreatment versus DMSO pretreatment; $P < 0.01$) (Fig. 6*C*). This antagonist effect was not a general effect of NAAs, because none of the other NAAs tested produced an equivalent antagonist response to C18:1-Gln (Fig. 6*C*). These data establish that TRPV1 is specifically antagonized by C18:1-Gln. Furthermore, because the

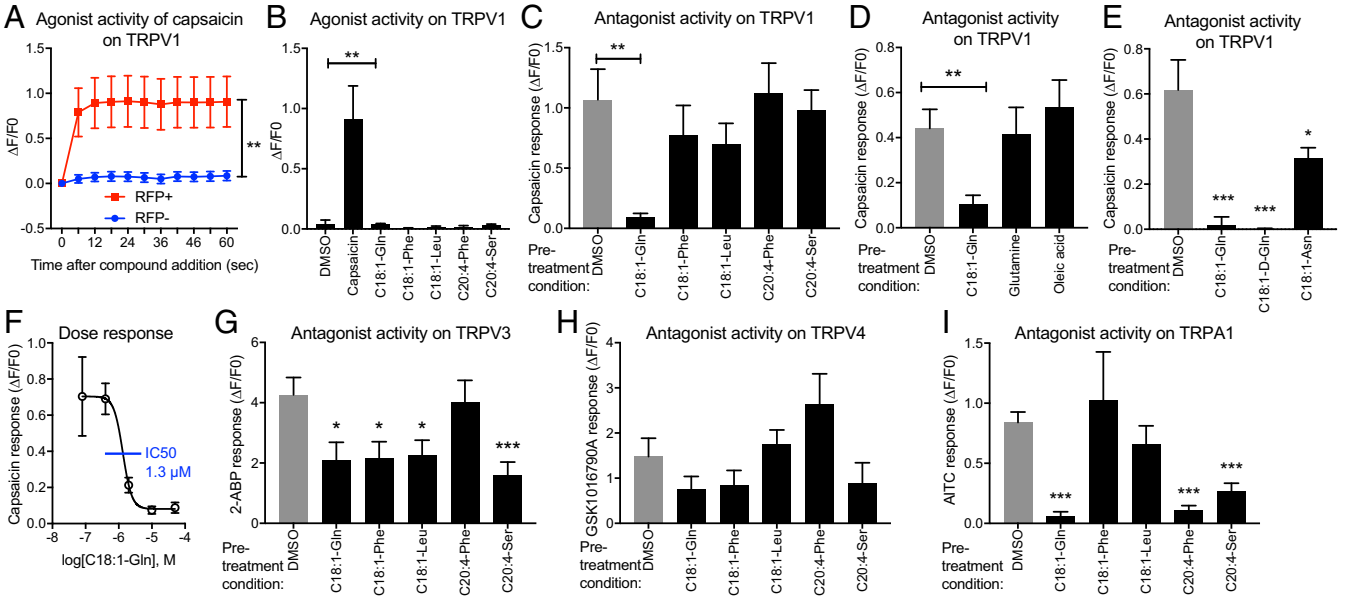

Fig. 6. Antagonism of TRP channels by PM20D1-regulated C18:1-Gln. (*A*) Change in relative Fluo-4 fluorescence ($\Delta F/F_0$) over time in cells transfected with TRPV1 (RFP^+) or in neighboring untransfected cells (RFP^-) following treatment with capsaicin. (*B*) Agonist response ($\Delta F/F_0$) in TRPV1-transfected cells after treatment with capsaicin or the indicated NAA (50 μM). (*C–E*) Antagonism of capsaicin-induced $\Delta F/F_0$ by the indicated compound (50 μM) in TRPV1-transfected cells. (*F*) Dose response of C18:1-Gln antagonizing capsaicin-induced $\Delta F/F_0$ in TRPV1-transfected cells. (*G–I*) Antagonism of agonist-induced $\Delta F/F_0$ by the indicated compound (50 μM) in TRPV3- (*G*), TRPV4- (*H*), or TRPA1- (*I*) transfected cells. For *A–I*, transfection was performed in HEK293A cells. For *C–I*, antagonist studies were performed by preincubating the indicated compound for 2 min. Agonist-induced $\Delta F/F_0$ was then quantified 1 min after addition of capsaicin (10 μM) or AITC (10 μM) or 12 s after addition of 2-ABP (500 μM) or GSK1016790A (0.2 μM). Data are shown as means ± SEM, $^*P < 0.05$, $^{**}P < 0.01$, $^{***}P < 0.001$ for the indicated comparison, or versus the corresponding DMSO control group. Fifteen to thirty cells were quantified per data point.

stimulation of cellular respiration is comparable between C18:1-Gln and these other NAAs (*SI Appendix*, Fig. S4), the C18:1-Gln/TRPV1 antagonist effect is likely independent of the previously reported mitochondrial uncoupling action of NAAs.

Structural Requirements and Generality of NAA Antagonism of TRP Channels. The structural requirements of C18:1-Gln for its antagonist effects were investigated. First, only the C18:1-Gln conjugate, but not glutamine head group alone or the free oleic acid alone, possessed antagonist activity (Fig. 6*D*). Second, no amino acid chirality requirement was observed: Both the natural C18:1-Gln and the unnatural enantiomer C18:1-D-Gln fully antagonized capsaicin-induced TRPV1 calcium flux (Fig. 6*E*). Third, C18:1-Asn, which differs from C18:1-Gln by the absence of a single methylene (CH_2) group, was not nearly as effective (49 ± 7% versus 97 ± 3% reductions of capsaicin responses with C18:1-Asn and C18:1-Gln, respectively), demonstrating that small perturbations to the amino acid side chain can strongly affect the antagonist action of C18:1-Gln (Fig. 6*E*). Last, the antagonist effect of C18:1-Gln was dose responsive with IC_{50} = 1.3 μM (Fig. 6*F*).

To explore the generality of NAA antagonism across the TRP family, we cotransfected plasmids expressing RFP and TRPV3, TRPV4, or TRPA1 into HEK293A cells. The specificity of each of these other assays was validated using specific chemical agonists to the corresponding channel [2-aminoethoxydiphenyl borane (2-APB) for TRPV3, GSK1016790A for TRPV4, and allyl isothiocyanate (AITC) for TRPA1]. Once again, as expected, only channel-transfected, RFP^+ cells, but not untransfected, RFP^- cells, exhibited a calcium flux in response to the corresponding agonist (*SI Appendix*, Fig. S5). The same set of NAAs was then tested for antagonist activity. For TRPV3, none of the NAAs tested completely abrogated the 2-APB–induced calcium flux, although many showed partial antagonist effects (47–62% reductions by NAA pretreatment versus DMSO) (Fig. 6*G*). None of the NAAs antagonized TRPV4 (Fig. 6*H*). Last, nearly complete antagonism of AITC-induced TRPA1 calcium flux was observed with C18:1-Gln (94 ± 5% reduction) and C20:4-Phe (87 ± 5% reduction), and a partial antagonist response was observed with C20:4-Ser (68 ± 8% reduction), while the other NAAs were ineffective (Fig. 6*I*). Taken together, these data indicate that C18:1-Gln and other NAAs each possesses a specific and unique pattern of antagonism across the various TRP channels previously implicated in nociception.

C18:1-Gln Administration Recapitulates the Antinociceptive Effects in PM20D1-KO Mice. We next treated mice with C18:1-Gln itself and assessed their pain behaviors in response to capsaicin, a direct TRPV1 agonist, as well as to formalin and acetic acid, two stimuli to which the PM20D1-KO mice had previously shown antinociceptive behaviors. C18:1-Gln was selected due to physiologic regulation during pain states (Fig. 5*H*), its broad elevation across multiple PM20D1-KO tissues (Fig. 2), and its polypharmacologic antagonist activity on TRPV1 and TRPA1 (Fig. 6). First, to assess whether pharmacological doses of C18:1-Gln could act as a TRPV1 antagonist in vivo, C18:1-Gln was administered to mice (100 mg/kg, i.p.) 15 min before intraplantar injection of capsaicin (1.5 μg per paw). C18:1-Gln reduced capsaicin-induced flinching as measured both by the number of flinches (Fig. 7*A*) and the time spent licking the injected paw (Fig. 7*B*). Similarly, C18:1-Gln–treated mice exhibited 54 ± 9% reductions in pain behaviors in the late phase of the formalin assay compared with vehicle-treated mice ($P < 0.01$, Fig. 7*C*). Even more strikingly, nearly all constriction behaviors were abolished in C18:1-Gln–treated animals in the acetic acid constriction test (Fig. 7*D*). Administration of C18:1-Gln at these doses did not affect movement in an open field assay (Fig. 7*E*), demonstrating that these antinociceptive behaviors were not due to a decrease in locomotor activity. Therefore administration of C18:1-Gln exhibits TRPV1 antagonist action in vivo and is sufficient to recapitulate the antinociceptive behaviors of PM20D1-KO mice.

Discussion

The NAAs are a structurally diverse class of bioactive signaling lipids whose endogenous physiologic functions have largely remained uncharacterized. From pharmacological studies using the NAAs themselves, the largest body of literature has suggested putative roles in metabolic homeostasis and pain sensation. For instance, in metabolism, C20:4-Gly can act as an insulin secretagogue (10), C18:1-Gly increases food intake (18), and multiple NAAs, including C18:1-Phe and C18:1-Leu, can uncouple mitochondrial respiration and increase energy expenditure in mice (8). In the regulation of pain sensation, C20:4-Gly is antinociceptive in inflammatory (11) and neuropathic (20) pain models, while C16:0-Gly suppresses heat-invoked firing of nociceptive neurons and reduces thermal pain sensation (12). Besides these two areas, other reports suggest putative NAA functions in additional physiologic processes, including blood pressure regulation (14), bone health (13), and angiogenesis (15). Here, we have critically interrogated the endogenous physiologic function of a subset of NAAs in metabolism and pain sensation by genetically disrupting the circulating enzyme PM20D1.

The studies here establish PM20D1 as a dominant NAA hydrolase/synthase across mouse tissues. Our previous gain-of-function experiments using AAV-PM20D1 injection in mice suggested that this enzyme drives the biosynthesis of NAAs in vivo (8). Surprisingly, rather than a broad depletion of NAAs, PM20D1-KO mice instead exhibit a bidirectional dysregulation of NAAs. These data underscore the inherent dual synthase/hydrolase activities embodied within PM20D1 polypeptide itself. PM20D1-KO mice also have a distinct NAA metabolite profile compared with mice overexpressing

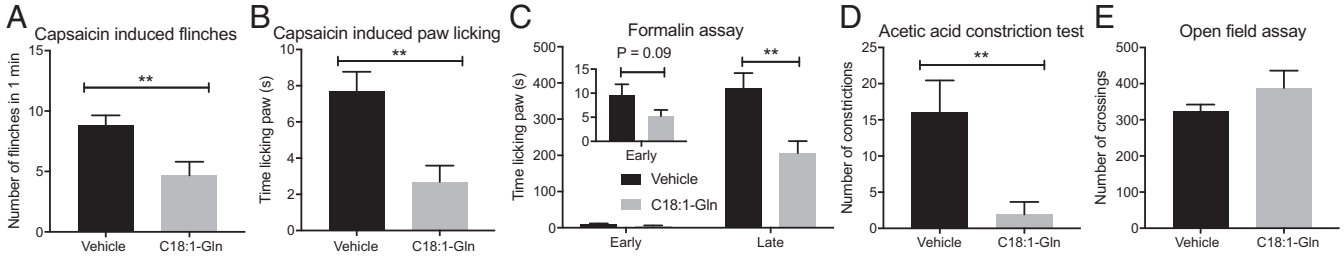

Fig. 7. C18:1-Gln exhibits antinociceptive bioactivity in vivo. (*A* and *B*) Number of flinches (*A*) and time spent licking the injected paw (*B*) after intraplantar administration of capsaicin (1.5 μg per paw). (*C*) Time spent licking the injected paw after intraplantar administration of 5% formalin (20 μL per paw). (*D*) Number of abdominal constrictions over 30 min following i.p. injection of 0.6% acetic acid (0.3 mL per mouse). (*E*) Total number of line crossings during a 5-min open field assay of 8- to 12-wk-old male wild-type mice treated with vehicle or C18:1-Gln (100 mg/kg, i.p.). C18:1-Gln was administered 15 min before the behavioral assays. Data are shown as means ± SEM; $^{**}P < 0.01$ for the indicated comparison; $n = 12$ per group.

PM20D1 (AAV-PM20D1 mice). For instance, C18:1-Phe was elevated in the blood of AAV-PM20D1 mice but was not changed in PM20D1-KO animals; conversely, circulating C18:1-Gln was increased in PM20D1-KO mice but was unchanged in AAV-PM20D1 mice versus control mice. The ultimate levels of NAAs in vivo are likely determined by a balance of PM20D1 localization as well as the concentrations of PM20D1 protein and the various NAA or fatty acid reactants. There may also be additional components that can alter the relative levels of NAAs, such as PM20D1-binding proteins in plasma or transporters that control the import/export of NAAs between tissues and blood.

Our studies also demonstrate a complex role for PM20D1-regulated NAAs in the control of metabolic and thermal homeostasis. PM20D1-KO mice are significantly more glucose intolerant and insulin resistant than WT mice following diet-induced obesity. They also exhibit enhanced defense of body temperature in cold. Given the polypharmacologic actions of C18:1-Gln and other NAAs in both mitochondrial uncoupling and TRP channel antagonism, a combination of multiple NAAs in distinct pathways might explain the altered metabolic parameters in PM20D1-KO mice. For instance, because TRPV1 antagonists elevate body temperature (27), the augmented body temperature in cold might reflect a combination of direct chemical uncoupling and/or antagonism of TRPV1 by NAAs. Similarly, TRPV1 and TRPA1 agonists have been shown to promote glucose tolerance; therefore the glucose intolerance may be due to a subset of elevated NAAs that antagonize TRP channels or a subset of depleted NAAs that function in mitochondrial uncoupling. A comprehensive analysis of similarities or differences in the various bioactivities of different NAAs, coupled with TRP channel-KO mice, will be ultimately required to clarify the potentially distinct functions of these lipids in vivo.

PM20D1-KO animals also exhibit a broad array of antinociceptive behaviors in response to chemical and inflammatory pain. These observations contribute to the previous pharmacological literature suggesting that Gly-containing NAAs (11) and other fatty acid derivatives (28, 29) can reduce pain behaviors when administered to mice. Mechanistically, C18:1-Gln appears to be a key PM20D1-regulated NAA that can recapitulate the antinociceptive behaviors observed in PM20D1-KO mice via antagonism of TRP channels. Importantly, the antagonist bioactivity of C18:1-Gln is specific to this lipid and not to the other NAAs tested, demonstrating that not all NAAs that can act as chemical uncouplers of mitochondrial respiration can function as TRP channel antagonists. Future work using purified, reconstituted TRP channels in defined membrane environments (30) could elucidate the precise interactions and mechanisms of the NAA–TRP channel interaction. Considering the unmet medical need for the treatment of pain (31), these data suggest that PM20D1 inhibitors, once they become available, might be useful as analgesic agents. Enhancing endogenous polypharmacologic antagonism of the TRP channels by blockade of a single enzyme could complement existing clinical efforts to develop direct TRP antagonists for pain treatment (32).

In summary, our studies using PM20D1-KO animals illuminate the control of metabolic homeostasis and nociceptive behaviors by PM20D1-regulated NAAs. Projecting forward, more extensive phenotyping of PM20D1-KO mice will likely uncover additional physiological processes regulated by NAA signaling in vivo. For instance, PM20D1 expression has recently been linked to Alzheimer's disease in humans (33), but the role of PM20D1 or NAA signaling in the central nervous system has not yet been fully explored. These future studies will also clarify the therapeutic areas in which augmentation or blockade of PM20D1 activity might be useful for the treatment of human disease.

Materials and Methods

Detailed methods for chemicals, molecular analysis, cell culture, and mass spectrometry are provided in *SI Appendix, SI Experimental Procedures*.

Chemicals and Materials. C20:4-Gly-d_8, C20:4-Ser, GSK1016790A, PGE_2, and the COX (ovine) Colorimetric Inhibitor Screening Assay Kit were purchased from Cayman Chemical Company; capsaicin, glutamine, phenylalanine, and oleic acid were purchased from Sigma; 2-APB was purchased from Santa Cruz Biotechnology; and C20:4-Phe was purchased from Abcam. The synthesis of C18:1-Phe, C18:1-Leu, C18:1-Gln, and C18:1-Lys has been described previously (8). Plasmids were obtained from the following sources: C-terminally tagged mouse TRPV1 (catalog no. MR227160; OriGene), C-terminally tagged human TRPV3 (catalog no. RC211184; OriGene); C-terminally tagged rat TRPV4 (plasmid no. 45751; Addgene); and pTurboRFP-Mito (catalog no. FP237; Evrogen). Mouse TRPA1 was a generous gift from Jorg Grandl, Duke University, Durham, NC. C2C12 cells and HEK293A cells were obtained from ATCC and Thermo Fisher Scientific, respectively.

General Animal Information. Animal experiments were performed according to procedures approved by the Beth Israel Deaconess Medical Center and The Scripps Research Institute Institutional Animal Care and Use Committee. The global PM20D1-KO mouse line will be available from The Jackson Laboratory as JAX#032193. Mice were maintained in 12-h light/dark cycles at 22 °C and were fed a standard irradiated rodent chow diet. All experiments on WT mice were performed with male C57BL/6J mice purchased from Jackson Laboratories (stock no. 000664). For experiments with PM20D1-KO mice, WT controls were all age- and sex-matched littermate animals. Full methods for the generation and phenotyping of PM20D1-KO mice are detailed in *SI Appendix, SI Experimental Procedures*.

Extraction of NAAs from Tissues. Frozen plasma (30 μL) was extracted in 160 μL of 1:1 (vol/vol) acetonitrile:methanol. Tissues were extracted in 500 μL 2:2:1 (vol/vol/vol) acetonitrile:methanol:water on a BeadBlaster homogenizer (Benchmark Scientific, Inc.) for 1 min. In both cases, 100 nmol of C15:0-Phe was included as an internal standard for absolute quantitation. Extracts were centrifuged at 5,000 × *g* for 10 min to remove debris. The supernatant was isolated and centrifuged again at 5,000 × *g* for 10 min. Finally, the twice-clarified supernatant was transferred to a mass spectrometry vial and analyzed by LC-MS as described in *SI Appendix, SI Experimental Procedures*.

Statistical Analysis. Student's *t* test was used for single comparison of mean values. Error bars represent ±SEM except when otherwise specified. $P < 0.05$ was considered to indicate statistical significance.

ACKNOWLEDGMENTS. We thank members of the B.M.S. laboratory, Y. Kutskova, D. Kole, and C. M. Hsieh (Abbvie Inc.) for helpful comments and discussions and J. Grandl for providing TRPA1 plasmids. This work was supported by NIH Grants DK105203 (to J.Z.L.), DK111916 (to K.J.S.), CA172667 (to D.K.N.), and DK31405 and DK061562 (to B.M.S.); American Cancer Society Research Scholar Award RSG14-242-01-TBE (to D.K.N.); the JPB Foundation (B.M.S.); and a Sponsored Research Agreement from Calico Life Sciences, LLC (B.M.S.).

1. Kappos L, et al.; FREEDOMS Study Group (2010) A placebo-controlled trial of oral fingolimod in relapsing multiple sclerosis. *N Engl J Med* 362:387–401.
2. McCormack K (1994) Non-steroidal anti-inflammatory drugs and spinal nociceptive processing. *Pain* 59:9–43.
3. Ahn K, et al. (2011) Mechanistic and pharmacological characterization of PF-04457845: A highly potent and selective fatty acid amide hydrolase inhibitor that reduces inflammatory and noninflammatory pain. *J Pharmacol Exp Ther* 338: 114–124.
4. Hanuš L, Shohami E, Bab I, Mechoulam R (2014) N-acyl amino acids and their impact on biological processes. *Biofactors* 40:381–388.
5. Devane WA, et al. (1992) Isolation and structure of a brain constituent that binds to the cannabinoid receptor. *Science* 258:1946–1949.
6. Cravatt BF, et al. (1995) Chemical characterization of a family of brain lipids that induce sleep. *Science* 268:1506–1509.
7. Tan B, et al. (2010) Identification of endogenous acyl amino acids based on a targeted lipidomics approach. *J Lipid Res* 51:112–119.
8. Long JZ, et al. (2016) The secreted enzyme PM20D1 regulates lipidated amino acid uncouplers of mitochondria. *Cell* 166:424–435.
9. Cohen LJ, et al. (2017) Commensal bacteria make GPCR ligands that mimic human signalling molecules. *Nature* 549:48–53.
10. Ikeda Y, et al. (2005) Identification of N-arachidonylglycine, U18666A, and 4-androstene-3,17-dione as novel insulin secretagogues. *Biochem Biophys Res Commun* 333:778–786.
11. Huang SM, et al. (2001) Identification of a new class of molecules, the arachidonyl amino acids, and characterization of one member that inhibits pain. *J Biol Chem* 276: 42639–42644.

12. Rimmerman N, et al. (2008) N-palmitoyl glycine, a novel endogenous lipid that acts as a modulator of calcium influx and nitric oxide production in sensory neurons. *Mol Pharmacol* 74:213–224.
13. Smoum R, et al. (2010) Oleoyl serine, an endogenous N-acyl amide, modulates bone remodeling and mass. *Proc Natl Acad Sci USA* 107:17710–17715.
14. Milman G, et al. (2006) N-arachidonoyl L-serine, an endocannabinoid-like brain constituent with vasodilatory properties. *Proc Natl Acad Sci USA* 103:2428–2433.
15. Zhang X, Maor Y, Wang JF, Kunos G, Groopman JE (2010) Endocannabinoid-like N-arachidonoyl serine is a novel pro-angiogenic mediator. *Br J Pharmacol* 160: 1583–1594.
16. Raboune S, et al. (2014) Novel endogenous N-acyl amides activate TRPV1-4 receptors, BV-2 microglia, and are regulated in brain in an acute model of inflammation. *Front Cell Neurosci* 8:195.
17. Console-Bram L, et al. (2017) N-arachidonoyl glycine, another endogenous agonist of GPR55. *Biochem Biophys Res Commun* 490:1389–1393.
18. Wu J, et al. (2017) N-oleoylglycine-induced hyperphagia is associated with the activation of agouti-related protein (AgRP) neuron by cannabinoid receptor type 1 (CB1R). *J Agric Food Chem* 65:1051–1057.
19. Succar R, Mitchell VA, Vaughan CW (2007) Actions of N-arachidonyl-glycine in a rat inflammatory pain model. *Mol Pain* 3:24.
20. Vuong LA, Mitchell VA, Vaughan CW (2008) Actions of N-arachidonyl-glycine in a rat neuropathic pain model. *Neuropharmacology* 54:189–193.
21. Sheskin T, Hanus L, Slager J, Vogel Z, Mechoulam R (1997) Structural requirements for binding of anandamide-type compounds to the brain cannabinoid receptor. *J Med Chem* 40:659–667.
22. Caterina MJ, et al. (2000) Impaired nociception and pain sensation in mice lacking the capsaicin receptor. *Science* 288:306–313.
23. Bang S, Yoo S, Yang TJ, Cho H, Hwang SW (2012) 17(R)-resolvin D1 specifically inhibits transient receptor potential ion channel vanilloid 3 leading to peripheral antinociception. *Br J Pharmacol* 165:683–692.
24. Alessandri-Haber N, et al. (2003) Hypotonicity induces TRPV4-mediated nociception in rat. *Neuron* 39:497–511.
25. McNamara CR, et al. (2007) TRPA1 mediates formalin-induced pain. *Proc Natl Acad Sci USA* 104:13525–13530.
26. Caterina MJ, et al. (1997) The capsaicin receptor: A heat-activated ion channel in the pain pathway. *Nature* 389:816–824.
27. Othman AA, Nothaft W, Awni WM, Dutta S (2013) Effects of the TRPV1 antagonist ABT-102 on body temperature in healthy volunteers: Pharmacokinetic/pharmacodynamic analysis of three phase 1 trials. *Br J Clin Pharmacol* 75:1029–1040.
28. Cravatt BF, et al. (2001) Supersensitivity to anandamide and enhanced endogenous cannabinoid signaling in mice lacking fatty acid amide hydrolase. *Proc Natl Acad Sci USA* 98:9371–9376.
29. Park CK, et al. (2011) Resolvin D2 is a potent endogenous inhibitor for transient receptor potential subtype V1/A1, inflammatory pain, and spinal cord synaptic plasticity in mice: Distinct roles of resolvin D1, D2, and E1. *J Neurosci* 31:18433–18438.
30. Cao E, Cordero-Morales JF, Liu B, Qin F, Julius D (2013) TRPV1 channels are intrinsically heat sensitive and negatively regulated by phosphoinositide lipids. *Neuron* 77: 667–679.
31. Gaskin DJ, Richard P (2012) The economic costs of pain in the United States. *J Pain* 13: 715–724.
32. Patapoutian A, Tate S, Woolf CJ (2009) Transient receptor potential channels,Targeting pain at the source. *Nat Rev Drug Discov* 8:55–68.
33. Sanchez-Mut JV, et al. (2018) PM20D1 is a quantitative trait locus associated with Alzheimer's disease. *Nat Med* 24:598–603.